

BLUE HORIZONTAL-BRANCH STARS IN THE SLOAN DIGITAL SKY SURVEY. I. SAMPLE SELECTION AND STRUCTURE IN THE GALACTIC HALO

EDWIN SIRKO,¹ JEREMY GOODMAN,¹ GILLIAN R. KNAPP,¹ JON BRINKMANN,² ŽELJKO IVEZIĆ,¹ EDWIN J. KNERR,^{1,3}
 DAVID SCHLEGEL,¹ DONALD P. SCHNEIDER,⁴ AND DONALD G. YORK⁵

Received 2003 August 13; accepted 2003 November 14

ABSTRACT

We isolate samples of 733 bright ($g < 18$) and 437 faint ($g > 18$) high Galactic latitude blue horizontal-branch stars with photometry and spectroscopy in the Sloan Digital Sky Survey (SDSS). Comparison of independent photometric and spectroscopic selection criteria indicates that contamination from F and blue straggler stars is less than 10% for bright stars ($g < 18$) and about 25% for faint stars ($g > 18$), and this is qualitatively confirmed by proper motions based on the USNO-A catalog as first epoch. Analysis of repeated observations shows that the errors in radial velocity are $\approx 26 \text{ km s}^{-1}$. A relation between absolute magnitude and color is established using the horizontal branches of halo globular clusters observed by SDSS. Bolometric corrections and colors are synthesized in the SDSS filters from model spectra. The redder stars agree well in absolute magnitude with accepted values for RR Lyrae stars. The resulting photometric distances are accurate to about 0.2 mag, with a median of about 25 kpc. Modest clumps in phase space exist and are consistent with the previously reported tidal stream of the Sagittarius dwarf galaxy.

Key words: Galaxy: halo — Galaxy: structure — stars: horizontal-branch

On-line material: machine-readable table

1. INTRODUCTION

Blue horizontal-branch (BHB) stars have long been important objects of study as tracers of the Galactic potential (Pier 1983; Sommer-Larsen, Christensen, & Carter 1989; Clewley et al. 2002). Their constant absolute magnitude allows accurate space positions to be determined. Historically, many researchers have used samples of BHB stars or other standard-candle stars, such as RR Lyraes, to study the local halo, i.e., the vicinity of the solar neighborhood, where typical distances are on the order of the solar Galactocentric radius $R_0 = 8 \text{ kpc}$. These samples can be used to constrain the kinematics of the local halo (Pier 1984; Layden et al. 1996). The distant halo (i.e., typical distances $\gg R_0$), however, is less well constrained (but see Sommer-Larsen et al. 1997). Isolating a sample of distant BHB stars would enable study of the structure and kinematics of the Galactic halo on larger scales (Sirko et al. 2004, hereafter Paper II) and estimates of the mass of the Galaxy.

The Sloan Digital Sky Survey (SDSS), currently halfway through a photometric and spectroscopic survey of a quarter of the sky, offers an excellent opportunity to isolate and study BHBs. The SDSS spectroscopic survey targets objects between about $g = 15.5$ and 19 (the bright limit is set to avoid contamination in adjacent spectroscopic fibers at the slit end of the fiber bundle), although a significant number of stars outside this range is also observed. Thus, BHB stars at distances from ~ 7 to $\sim 60 \text{ kpc}$ from the Sun appear in the spectroscopic survey.

This paper presents 1170 BHB stars selected from SDSS that probe the outer halo. The plan of the paper is as follows. Pertinent characteristics of the SDSS are summarized in § 2. Section 3 describes the preliminary color cut. Section 4 discusses spectroscopic BHB classification criteria. For the faint stars, the spectroscopic classification breaks down so we resort to a more stringent color cut described in § 5. Radial velocity errors are evaluated in § 6. Section 7 discusses the calculation of bolometric corrections for accurate distances and evaluates magnitude errors. Some sanity checks are presented in § 8, including an analysis of the limited proper motion data available and a map of the Galactic halo, which shows the conspicuous Sagittarius tidal stream (Fig. 13). The results are summarized in § 9. The sample is available in Table 3.

2. THE SLOAN DIGITAL SKY SURVEY

The SDSS (York et al. 2000) is a project to image about one-quarter of the sky at high Galactic latitude to a depth of about 21–22 mag in five broad bands covering the entire optical range and to obtain spectra of about a million galaxies and 100,000 quasars selected from the imaging data. While galaxies and quasars are the primary targets of the spectroscopic survey, the SDSS also obtains a vast amount of stellar data. Stellar spectra are acquired by several routes: observations of calibration stars, observations of various classes of stars to be used as “filler” observations when a given region of sky has too low a density of primary targets, and via objects targeted as candidate galaxies and quasars that turn out to be stars.

The SDSS uses a dedicated 2.5 m telescope and a large format CCD camera (Gunn et al. 1998) at the Apache Point Observatory in New Mexico to obtain images almost simultaneously in five broad bands (u, g, r, i, z) centered at 3551, 4686, 6166, 7480, and 8932 Å, respectively (Fukugita et al. 1996; Gunn et al. 1998). The imaging data are automatically processed through a series of software pipelines that find and

¹ Princeton University Observatory, Peyton Hall, Princeton, NJ 08544.

² Apache Point Observatory, P.O. Box 59, Sunspot, NM 88349.

³ University of Minnesota, Law School, 229 19th Avenue South, Minneapolis, MN 55455.

⁴ Department of Astronomy and Astrophysics, Pennsylvania State University, 525 Davey Laboratory, University Park, PA 16802.

⁵ Department of Astronomy and Astrophysics, University of Chicago, 5640 South Ellis Avenue, Chicago, IL 60637.

measure objects and provide photometric and astrometric calibrations to produce a catalog of objects with calibrated magnitudes, positions, and structure information. The photometric pipeline PHOTO (Lupton et al. 2001) detects the objects, matches the data from the five filters, and measures instrumental fluxes, positions, and shape parameters. The last allows the classification of objects as “point source” (compatible with the point-spread function [PSF]) or “extended.” The instrumental fluxes are calibrated via a network of primary and secondary stellar flux standards to AB_r magnitudes (Fukugita et al. 1996; Hogg et al. 2001; Smith et al. 2002). We use the “PSF magnitude,” which represents the magnitude of the best-fit PSF to the object, as determined by PHOTO version 5.4.25 (2003 June). The PSF magnitudes are currently accurate to about 2% in g , r , and i and 3%–5% in u and z for bright (<20 mag) point sources. The SDSS is 50% complete for point sources to $(u, g, r, i, z) = (22.5, 23.2, 22.6, 21.9, 20.8)$, and the full width at half maximum (FWHM) of the PSF is about 1".5 (Abazajian et al. 2003). The data are saturated at about 14 mag in g , r , and i and about 12 mag in u and z . Astrometric calibration is carried out using a second set of less sensitive CCDs in the camera, which allows the transfer of astrometric catalog positions to the fainter objects detected by the main camera. Absolute positions are accurate to better than 0".1 in each coordinate (Pier et al. 2003).

The SDSS spectroscopic survey is carried out by targeting objects selected from the imaging catalogs according to predetermined and carefully tested criteria (Stoughton et al. 2002). The targeted stars, quasars and galaxies have limiting magnitudes of around 18–20 mag (Richards et al. 2002; Eisenstein et al. 2001; Strauss et al. 2002). BHB stars appear in the SDSS spectroscopic sample via two main routes. At redshifts around 2.7, the quasar color locus crosses the BHB color locus (Richards et al. 2002) and many BHB stars are targeted as candidate quasars. BHB stars are also photometrically selected to serve as filler observations in regions of the sky with a low density of primary targets. The sky locations of the target objects are mapped to a series of plug plates that feed a pair of double spectrographs via optical fibers. The spectrographs jointly observe 640 objects (including sky positions and standard stars) simultaneously, and provide continuous wavelength coverage from about 3800 to 9500 Å at a resolution of about 1800–2100. The nominal total exposure time for each spectroscopic plate is 45 minutes (15 minutes times three exposures), plus observations of flat field and arc standard lamps for every plate. The entrance aperture of the fibers is 3". The spectra are matched to the photometric objects using a video mapping system for the plug plates. The spectra are recorded on CCD detectors. The data are optimally extracted, the sky spectrum is subtracted, and wavelength, flat-field, and spectrophotometric calibrations are applied automatically by the SPECTRO-2D software pipeline.

Each spectroscopic plate is a circle of diameter 3° on the sky. The present work is based on the data of 937 unique spectroscopic plates taken to date, through 2003 August 6. In addition, 77 plates were observed redundantly, but in defining the BHB sample we exclude redundant observations by adopting the plate with the highest signal-to-noise ratio (S/N). However, we use the information from these redundant observations in § 6 below to evaluate velocity errors.

The radial velocity is found by fitting the spectrum to template spectra, using an automated fitting program (SPECTRO_BRIGHTSTARS) written by D. Schlegel. The basic procedure is as follows. Prugniel & Soubiran (2001) have published

a catalog of about a thousand spectra of stars with a wide range of properties (spectral types, metallicities, etc.) observed at high spectral resolution with the ELODIE spectrograph. One version of the ELODIE spectra is binned to $R \sim 20,000$ and spectrophotometrically calibrated to about 5%. BRIGHTSTARS was used to select template spectra from the SDSS data that match the ELODIE spectra. These template spectra are typically composites from many SDSS spectra and are set up to provide relatively coarse sampling of the spectral type grid. The template spectra are aligned to zero heliocentric velocity. Each SDSS spectrum is then compared with the template spectra in wavelength space, and the template and wavelength shift that give the best match is automatically measured. For the stars in the present sample the best-fit spectral types were almost all between B6 and A0. The radial velocities are corrected to the heliocentric standard of rest and throughout this paper are denoted v_r .

3. COLOR CUT

BHB stars have very characteristic colors in the high Galactic latitude stellar sample observed by the SDSS imaging survey, and photometric selection of candidate objects is straightforward. BHB stars are bluer in $g-r$ than most halo stars because the halo main-sequence turnoff lies at spectral type F/G. The large Balmer jump in BHB low-gravity stars gives them redder $u-g$ colors than other blue objects such as low-redshift quasars and white dwarfs, and indeed the SDSS u and g filters are specifically designed to provide optimal photometric separation of low-redshift quasars (Gunn et al. 1998; York et al. 2000; Richards et al. 2002). The SDSS $g-r$ versus $u-g$ color-color diagram in Figure 1 shows all objects in the spectroscopic sample of 937 plates used herein that were subsequently identified as stars by BRIGHTSTARS, which is accurate enough that quasars and galaxies are virtually nonexistent in the sample. (Throughout this paper all magnitudes are corrected for Galactic extinction using the maps of Schlegel, Finkbeiner, & Davis 1998.) The region occupied by BHB stars is indicated with a “color cut box,” with boundaries $0.8 < u-g < 1.35$,

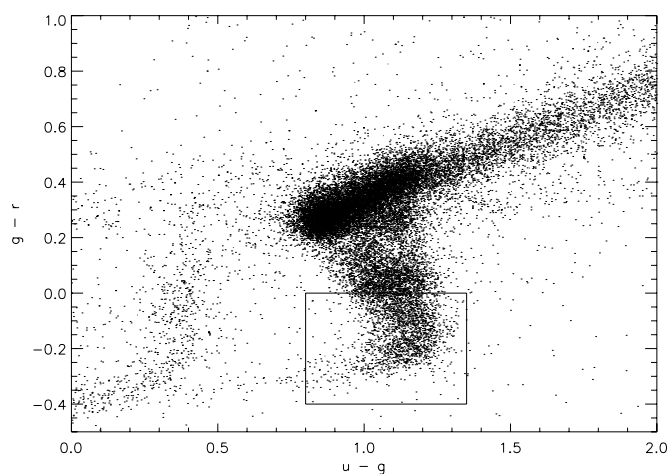


FIG. 1.—SDSS color-color diagram showing all spectroscopically targeted objects brighter than $g = 18$ (for clarity) that were subsequently confirmed as stars. The main sequence runs from the center of this diagram toward the upper right, and the large Balmer jump of A-colored stars places them in the offshoot, where our “color cut” selection box is drawn. Note that the relative densities of stars in this plot are affected by selection bias; for example, more stars appear here that lie in the more “interesting” regions of color-color space for QSOs.

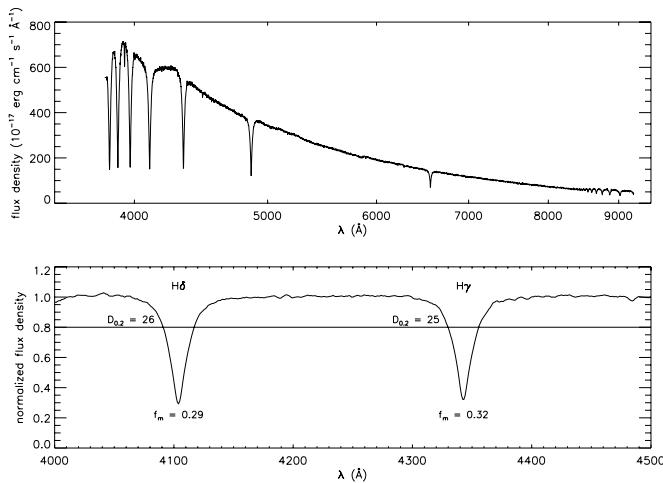


FIG. 2.—Spectrum of a typical (high S/N) BHB star (*top*) and the H γ -H δ region of the same star with the continuum divided out (*bottom*). The parameters (f_m , $D_{0.2}$) are labeled for both lines.

$-0.4 < g-r < 0.0$. The boundaries of this selection box are similar to those used by Yanny et al. (2000), and Figure 8 (see § 5) shows that our final sample of bright BHB stars is well contained within the boundaries. Stars that lie in this region of color-color space pass what we refer to as the “color cut.”

Although BHB stars are effectively selected through the color cut described above, there remains a significant degree of contamination from two other types of star. The locus of cooler F stars is actually quite outside of the color cut box, to the red in $g-r$ (Yanny et al. 2000), but there are so many F stars that they leak into the BHB candidate sample via intrinsic variations and photometric errors, with numbers comparable to the number of BHB stars. To identify these cooler stars merely requires a measure of temperature independent of $u-g$ or $g-r$. Somewhat more challenging to identify are the A-type stars with higher surface gravity (Preston & Sneden 2000; Yanny et al. 2000; Clewley et al. 2002). These are probably field blue straggler (BS) stars, which are some 2 mag less luminous (Preston & Sneden 2000). While the Balmer jump as measured by $u-g$ can separate out many of these stars, some remain in the sample. They can be removed using their broader Balmer lines as described in the next section.

4. BALMER LINE ANALYSIS CUTS

The top panel of Figure 2 presents a typical BHB spectrum, showing the deep Balmer lines of an A-type star. In this section we describe two methods for analyzing these lines: the widely used $D_{0.2}$ method (Pier 1983; Sommer-Larsen & Christensen 1986; Arnold & Gilmore 1992; Flynn, Sommer-Larsen, & Christensen 1994; Kinman, Suntzeff, & Kraft 1994; Wilhelm, Beers, & Gray 1999) and the scale width–shape method (Clewley et al. 2002). We focus on the H γ and H δ lines because the H β and H α lines have lower continuum levels and the lines above H δ are much more closely spaced, making the determination of the continuum difficult (Yanny et al. 2000).

To analyze the lines, the continuum must first be fitted and divided out. For the $D_{0.2}$ method, following Yanny et al. (2000), we assume that the continuum ranges from 4000 to 4500 Å with 60 Å masks covering the positions of the H γ and H δ lines. We then divide the spectrum by the best-fit sixth-order Legendre polynomial to this extracted continuum.

Finally, the spectrum is boxcar smoothed with a boxcar length of 5 pixels. An example normalized and extracted spectral energy distribution (SED) is shown in the lower panel of Figure 2. Similarly, for the scale width–shape method, we take the continuum extraction rule of Clewley et al. (2002; which ranges from 3863 to 4494 Å) and fit to a fourth-order Legendre polynomial. After the continuum is divided out with this prescription, the SED looks very similar to the example SED in the lower panel of Figure 2.

The following terminology is used in this section and throughout. A “method” refers to a general algorithm, which may or may not be desirable for isolated use, which employs one or more “criteria” for discriminating BHB stars. The $D_{0.2}$ method and the scale width–shape method are presented in the following. A “cut” is a method or combination of methods that we *actually* used to eliminate contaminants from the sample. The combination cut discussed below incorporates the $D_{0.2}$ and scale width–shape methods.

4.1. The $D_{0.2}$ Method

Since BHB stars have low surface gravity, their Balmer lines are narrower than the smaller main-sequence BS stars. The $D_{0.2}$ method discriminates BHB stars from BS stars by determining the value of $D_{0.2}$, the width in angstroms of the Balmer line at 80% of the continuum (Yanny et al. 2000). Figure 3 demonstrates how this parameter can discriminate a BHB from a BS star. Although simple, this method has been found to be fairly robust and can provide a better measurement of the line width than other more complicated procedures (e.g., Flynn, Sommer-Larsen, & Christensen 1994).

The $D_{0.2}$ method nominally applies only to objects with A-type spectra. However, as mentioned in § 3, a large contaminant of our sample is F stars. Since F-type stars have weaker Balmer lines than A-type stars, one way of measuring temperature is by measuring the depth of the H γ or H δ line. Here we define f_m as the flux relative to the continuum at the minimum of the line. Thus, higher values of f_m for the Balmer lines signify cooler stars. A plot of $D_{0.2}$ versus f_m for stars passing the color cut is shown in Figure 4. In this figure, only stars with g magnitudes less than 18 are shown, so that the trends in the plot are not obscured by the noise in the data from fainter stars (see Fig. 5, to be discussed in § 4.3).

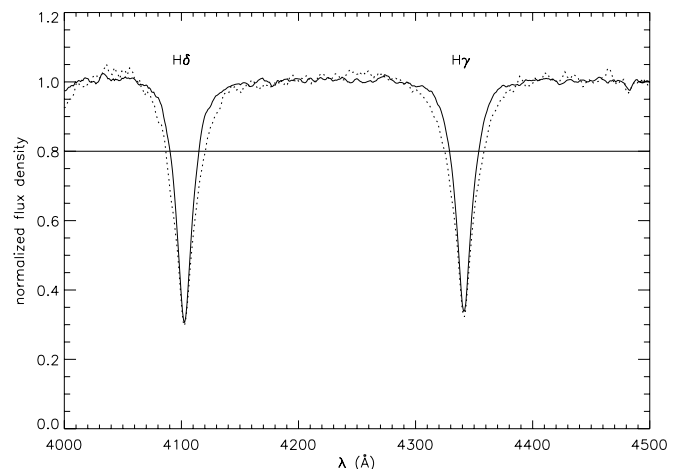


FIG. 3.—Extracted and normalized spectrum of a BHB star (*solid line*) and a BS star (*dotted line*) clearly showing the BS star’s wider Balmer lines at 80% of the continuum.

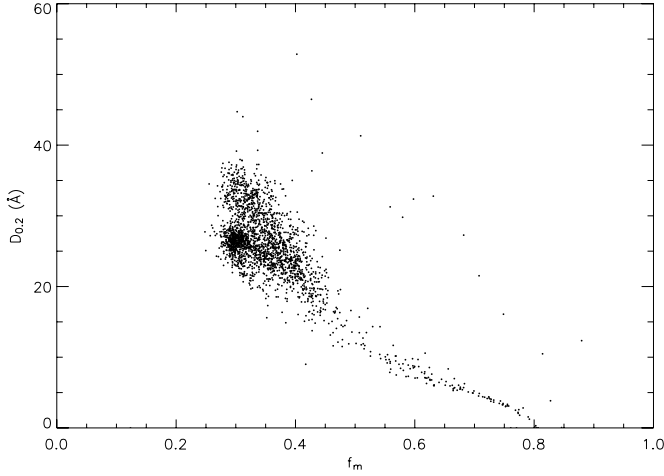


FIG. 4.—Parameters f_m and $D_{0.2}$ as determined by the $H\delta D_{0.2}$ method for stars that pass the color cut with $g < 18$. The trail of stars with $f_m \gtrsim 0.4$ are too cool to be BHB stars, and the concentration of stars with $D_{0.2} \gtrsim 28$ is due to BS stars with higher surface gravity. The ~ 10 stars that lie well above the main locus for $f_m \gtrsim 0.4$ are placed there by poor parameter determinations due to missing spectroscopic data at the location of the $H\delta$ line.

The concentration of stars near $(f_m, D_{0.2}) = (0.30, 26 \text{ \AA})$ represents the BHB stars, and those stars with larger values of $D_{0.2}$ are BS stars. Figure 4 also suggests that the locii of BS and BHB stars propagate to larger f_m and smaller $D_{0.2}$ until the two locii converge at about $(f_m, D_{0.2}) = (0.4, 23 \text{ \AA})$. In other words, for a given $0.3 \lesssim f_m \lesssim 0.4$, the distribution of stars in $D_{0.2}$ is bimodal, but the stars are most cleanly separated for the smaller values of f_m and not separated at all when $f_m \sim 0.4$. Even though Figure 4 does not show the trend clearly, we return to this point in § 4.3 and show that the stars with smaller values of $D_{0.2}$ but with $0.34 \lesssim f_m \lesssim 0.4$ are the other horizontal-branch stars; RR Lyrae stars, for example, fall into this region of the horizontal branch. Because horizontal-branch stars are evidently more difficult to discriminate from main-sequence stars at lower temperatures, we adopt the criteria $f_m < 0.34$, $D_{0.2} < 28$ for likely BHB stars for the $H\delta D_{0.2}$ method.

4.2. The Scale Width–Shape Method

Clewley et al. (2002) have proposed the scale width–shape method for discriminating BHB stars based on the Sérsic profile for Balmer lines (Sérsic 1968):

$$y = 1.0 - a \exp \left[- \left(\frac{|x - x_0|}{b} \right)^c \right]. \quad (1)$$

Here y is the normalized flux and x is the wavelength in angstroms. We fit the normalized extracted spectrum (where the bounds of extraction are given by Clewley et al. 2002) to the Sérsic profile with three free parameters: a , b , and c . The parameter x_0 is assumed to be the nominal location of the Balmer line corrected for redshift, which has already been determined. After fitting both Balmer lines of every star to the three-parameter (a, b, c) Sérsic profile, there is a reasonably small dispersion in the determination of a : for the $H\gamma$ line the average is 0.690 and the rms is 0.019; for $H\delta$ the average is 0.740 and the rms is 0.018. We fix a at its average value among stars passing the BHB criteria of the $H\delta D_{0.2}$ method, which is not objectionable because the $D_{0.2}$ method is independent of the scale width–shape method. The Balmer

lines are then refitted to the two-parameter (b, c) Sérsic profile. This refitting is important because errors in a are correlated with the errors in b and c (Clewley et al. 2002). For this work we adopt $a_\gamma = 0.690$ for the $H\gamma$ line and $a_\delta = 0.740$ for the $H\delta$ line. The optimum value of a most likely depends on the resolution of spectroscopy and similar factors.

Fitting to the Sérsic profile thus provides the two parameters b and c for both the $H\gamma$ and $H\delta$ lines, for every star. Clewley et al. (2002) show that BHB and BS stars separate rather cleanly in a plot of b against c . Furthermore, they show that c is a measure of temperature: cooler stars have smaller values of c .

4.3. Determination of Criteria for the $D_{0.2}$ and Scale Width–Shape Methods

We concentrate on the set of brighter stars with $g < 18$ because the noise in the spectra of fainter stars throws large errors in the parameter determinations for the $D_{0.2}$ method and the scale width–shape method. This point is illustrated in Figure 5. We will return to the selection of BHBs from the fainter star sample in § 5.

Figure 6 shows the parameters of the sample of BHB candidates with $g < 18$ as determined by the two line width analysis methods described in the preceding sections. Each star is represented by the same color in all four panels. In this figure the $H\delta D_{0.2}$ method is represented in the lower left panel, and stars that pass the BHB criteria for this method are colored blue, stars that are likely BS stars are green, and all others (cooler stars) are red. It is readily apparent that the four *independent* parameter spaces map BHB stars, BS stars, and cool stars to different regions.

The exact BHB criteria for each method were determined through a combination of adjusting the bounds of the criteria by eye and comparing the results of one method to the others. For instance, the scale width–shape method separates BHB and BS stars cleanly enough that there is a natural gap between the two distributions in a plot of b versus c , as shown in Figure 6. A parabola is qualitatively drawn to divide the two distributions. Similarly, with regard to the $D_{0.2}$ method, the distribution in $D_{0.2}$ of the stars with low values of f_m naturally separates into the two populations of BHB and BS stars. The issue of where to draw the temperature criterion (f_m for the $D_{0.2}$ method and c for the scale width–shape method) is more sensitive because the “natural” gap is harder to see in the $D_{0.2}$ method and seems to be nonexistent in the scale width–shape method. In fact, the top right panel of Figure 6 hints that the division between stars with low surface gravity and high surface gravity continues even for much cooler stars than BHB stars. The cooler population ($0.8 \lesssim c_\gamma \lesssim 1.0$) with lower surface gravity (lower b_γ) is thus the horizontal-branch stars that are not blue, e.g., RR Lyrae stars. This b versus c plot corroborates the evidence in § 4.1 that nonblue horizontal-branch stars form a locus in the $(f_m, D_{0.2})$ -plane, which extends out to cooler temperatures corresponding to $f_m \sim 0.4$. Figure 7 shows that the stars of the population that has smaller values of b_γ also have smaller values of $D_{0.2}$. With this information, we deduce that the BHB stars are located in the clump in the $H\delta f_m$ – $D_{0.2}$ plane centered on $(f_m, D_{0.2})_{H\delta} \sim (0.30, 26 \text{ \AA})$ and we set the temperature criterion at $f_m = 0.34$. A subsequent inspection of Figure 6 reveals that most BHB stars have $c_\gamma > 1.0$, so we adopt this as the temperature criterion for the $H\gamma$ scale width–shape method. Table 1 lists the adopted BHB selection criteria for each method.

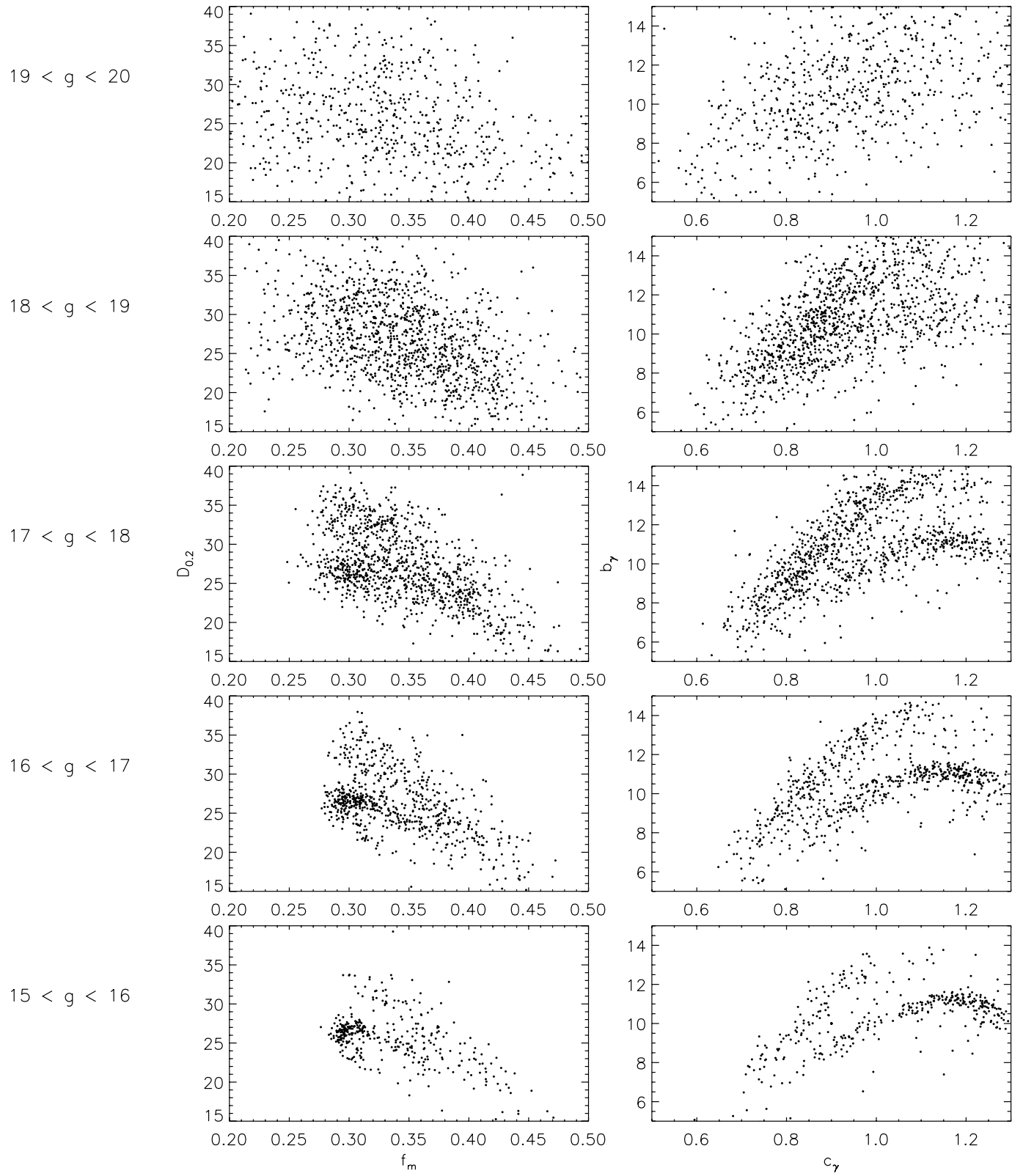


FIG. 5.—Parameter determinations of the $H\delta D_{0.2}$ method (*left*) and of the $H\gamma$ scale width–shape method (*right*) for five g magnitude bins, labeled. Errors evidently become too large to safely discriminate BHB stars from other types of stars at about $g \sim 18$.

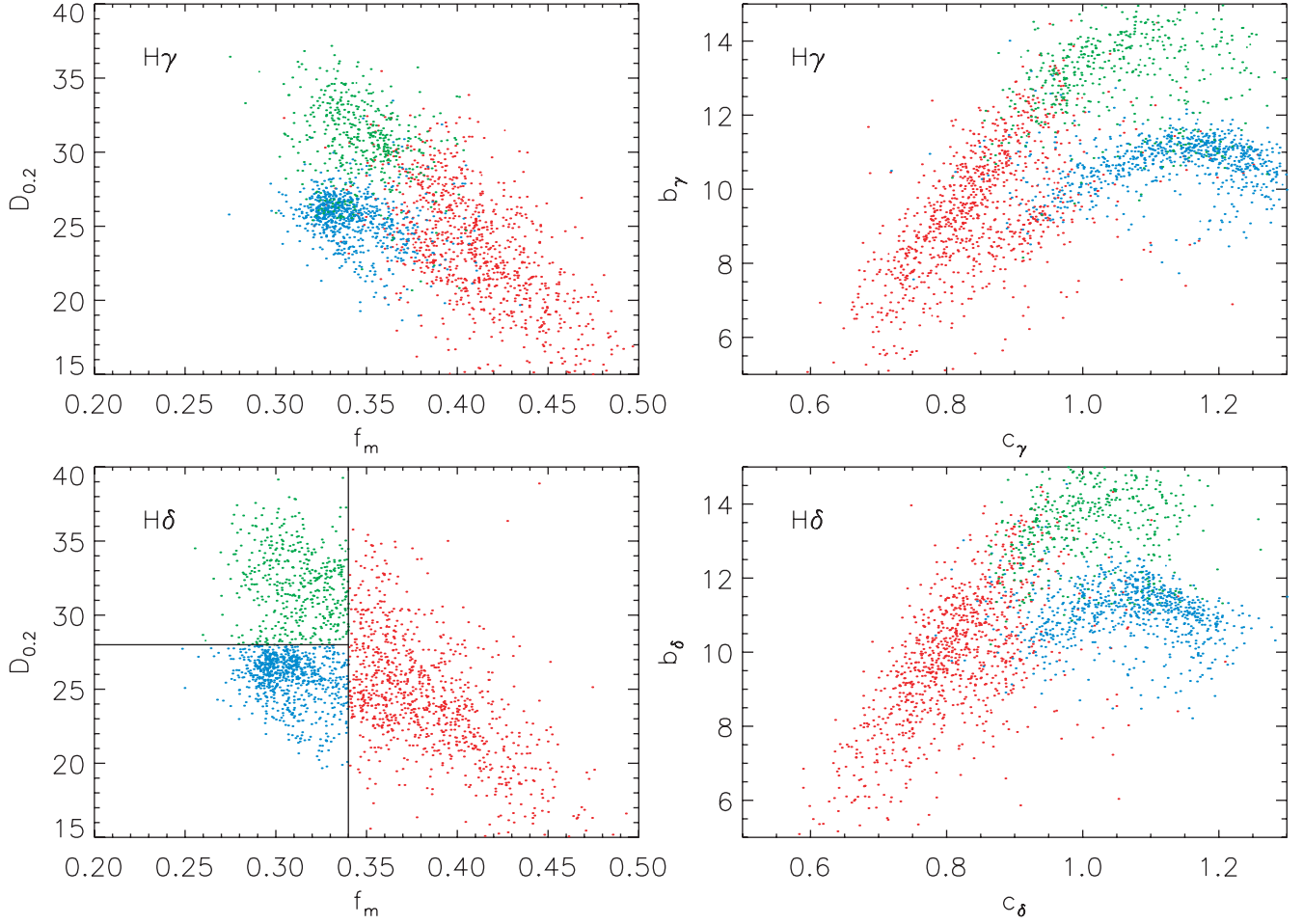


FIG. 6.—Comparison between the $D_{0.2}$ method (left) and the scale width–shape method (right) for the $H\gamma$ line (top) and the $H\delta$ line (bottom). Each star is represented by the same color in all four plots, so the compatibility among all four methods is seen. Here stars are colored according to their classification by the $D_{0.2}$ method for the $H\delta$ line: BHB stars are blue, BS stars are green, and the cooler stars are red. Only stars with $g < 18$ are plotted here.

4.4. The Combination Cut

We define the combination cut as those stars that pass the criteria for the $H\gamma D_{0.2}$ and $H\delta$ scale width–shape methods *or* the $H\delta D_{0.2}$ and $H\gamma$ scale width–shape methods. We assume that the $H\gamma D_{0.2}$ and $H\delta$ scale width–shape methods are completely independent of each other, as are the $H\delta D_{0.2}$ and $H\gamma$ scale width–shape methods. This assumption is reasonable because no information is shared in the analyses of either line, and the $D_{0.2}$ and scale width–shape methods measure fundamentally different properties of the spectral energy distribution. Under this assumption, the contamination fraction for the combination cut would be $\kappa_{\text{combo}} \approx 2\kappa^2$, where κ is the contamination fraction of a single method. In the Appendix we show that the contamination fraction of any one of the four methods is probably $\kappa \lesssim 10\%$, so $\kappa_{\text{combo}} \lesssim 2\%$ under these assumptions. However, to be more conservative, the fact that $\kappa \sim 10\%$ for all four individual methods suggests that κ_{combo} is probably 10% or less; in Paper II we use $\kappa_{\text{combo}} = 10\%$ to study errors introduced by contamination into the kinematic analysis.

5. THE FAINTER STARS

As shown in Figure 5, the line width analysis methods cannot be expected to perform accurately for stars fainter than $g \gtrsim 18$; in fact the number of $g > 18$ stars that are identified differently in any two methods (~ 100 – 400) is of the same

order as the number of $g > 18$ stars identified as BHB stars in one method (~ 200 – 500). Because these fainter stars have noisier spectra, not only are the algorithmic BHB criteria unreliable, but eye inspection would be difficult at best. However, an inspection of the results of the combination cut applied to the bright ($g < 18$) stars, as shown in Figure 8, reveals that BHB stars, BS stars, and cooler stars occupy different regions of color-color space, although there is significant overlap. In this figure BHB stars are defined as those that pass the combination cut; (green) BS stars are defined as those that do not pass the combination cut but lie in the BS region for the $H\delta D_{0.2}$ method; and red stars are everything else. The thick curved line with periodic circles will be explained in § 7.

The bounds of this particular plot are the same as the color cut discussed in § 3, so it is evident that the BHB stars are more likely to be found in the region enclosed by the “piano” shape indicated than outside of it. Since SDSS photometry can be expected to be accurate to a fainter magnitude ($g \sim 20$; York et al. 2000) than can the combination method (see Fig. 5), we select BHB stars with $g > 18$ solely on the basis of color. The new color cut is indicated by the piano shape in Figure 8 (and is given by the region $0.85 < u-g < 1.3$, $-0.31 < g-r < -0.13$ excluding the elliptical subregion $[(u-g-0.85)/0.31]^2 + [(g-r+0.13)/0.11]^2 < 1$) and will be referred to here as the “stringent” color cut.

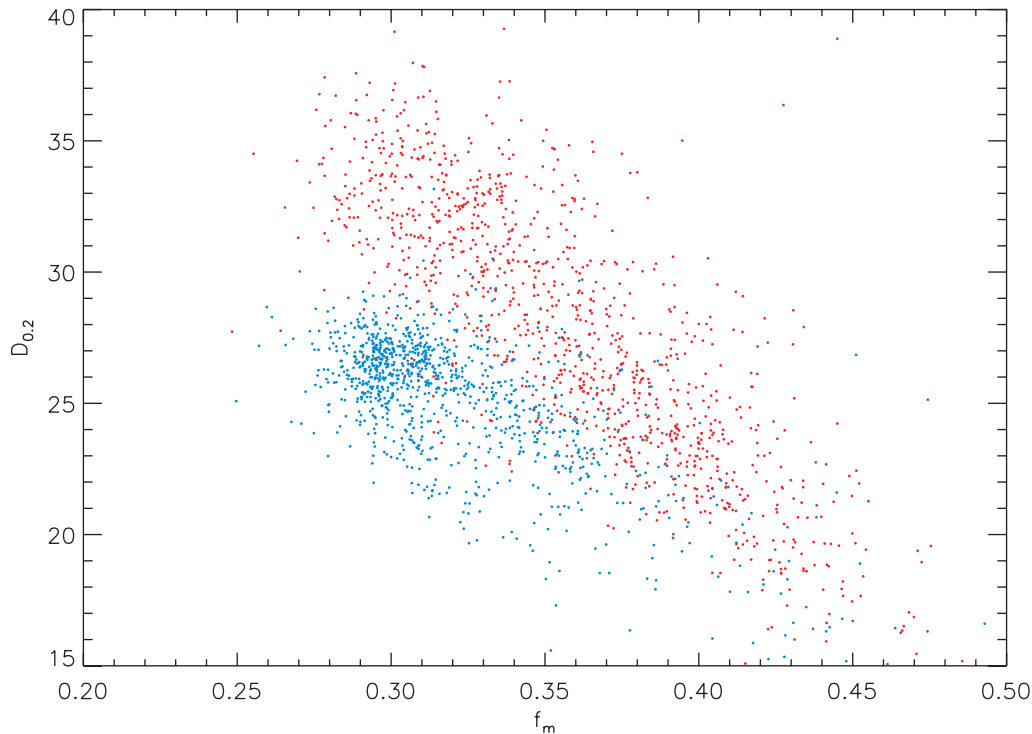


FIG. 7.—Parameter determinations from the $H\delta D_{0.2}$ method for stars with $g < 18$. Stars are colored according to their location on the b – c diagram for the $H\gamma$ scale width–shape method: stars for which $b < 12 - 30(c - 1.18)^2$ are blue; all others are red. (The temperature criterion is not used.) Thus, stars that have low values for b from the scale width–shape method also have low values for $D_{0.2}$ and are likely horizontal-branch stars.

What are the contamination and incompleteness for the stringent color cut with no spectroscopic analysis? Assuming that the combination cut is 100% accurate for $g < 18$, there are 733 BHB stars, 172 of which do not pass the stringent color cut. There are 199 stars that pass the stringent color cut that are not classified as BHB stars by the combination method. Most of these (133) are classified as BS stars by the $H\delta D_{0.2}$ method. Thus, the contamination for the stringent color cut alone is $199/(733 - 172 + 199) \approx 25\%$.

6. DUPLICATE STARS AND RADIAL VELOCITY ERRORS

Since the spectroscopic plates overlap on the sky, sometimes objects are targeted for spectroscopy on two different plates. Of the 4515 stars passing the color cut (from *unique* plates), 81 are duplicate observations of the same star on different plates. We remove these 81 redundant observations from our BHB sample. In addition, from the data of the 77 nonunique plates (see § 2), there are 410 stars passing the color cut that duplicate observations of stars from the unique plates. Each spectroscopic observation of a star provides an independent measurement of radial velocity v_r and, for the bright ($g < 18$) stars, an independent classification as a BHB

star or non-BHB star. Figure 9 shows the 491 stars that have multiple spectra and therefore independent determinations of v_r . The ordinate axis shows the difference in the radial velocity determinations Δv_r between each duplicate star and its corresponding star in our purified sample of unique stars. Stars that are classified as BHBs for both observations are colored blue, stars that are classified as non-BHBs for both observations are colored red, and stars that have conflicting classifications between the two observations are colored green. Brighter than $g = 18$, there are 91 stars that are doubly classified as BHBs, 131 stars that are doubly classified as non-BHBs, and 13 stars that have conflicting classifications. This is consistent with the 10% contamination determined in the Appendix, assuming that there is about an equal number of contaminants in the BHB sample as the number of BHB stars that are not classified as such (i.e., assuming $\kappa \approx \eta$). Figure 9 also shows the dependence of velocity errors on magnitude; as expected, fainter stars tend to have greater velocity errors, presumably due to noisier spectra. The rank correlation coefficient of $(g, |\Delta v_r|)$ is 0.263. The velocity differences determined this way turn out to be consistent with the errors derived from the spectral fits for only about half of the stars, independent of the magnitude or whether or not a star is a

TABLE 1
BHB CRITERIA FOR THE DIFFERENT METHODS

Method	Temperature Criterion	Line width Criterion
$D_{0.2}$ method ($H\gamma$).....	$f_m < 0.37$	$D_{0.2} < 28 \text{ \AA}$
$D_{0.2}$ method ($H\delta$).....	$f_m < 0.34$	$D_{0.2} < 28 \text{ \AA}$
Scale width–shape method ($H\gamma$).....	$c > 1.00$	$b < 12.0 - 30(c - 1.18)^2$
Scale width–shape method ($H\delta$).....	$c > 0.95$	$b < 12.5 - 40(c - 1.10)^2$

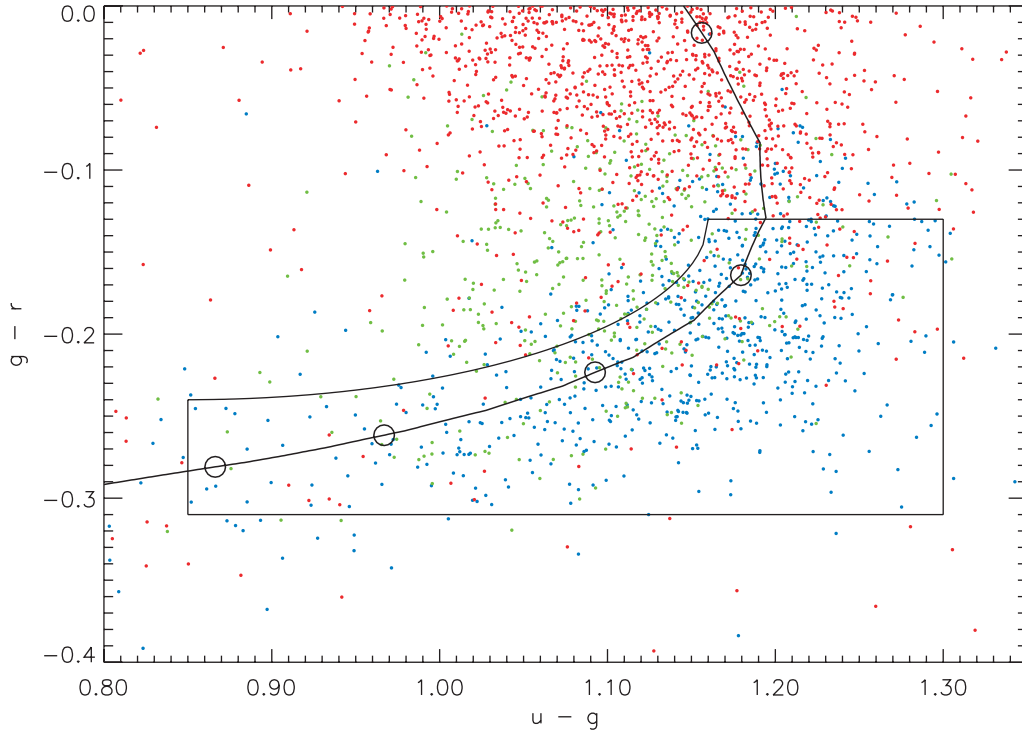


FIG. 8.—Same diagram as Fig. 1, but a close-up of the color cut box and with stars colored according to their determined classifications by the combination cut. Only stars with $g < 18$ are shown. BHB stars are blue, BS stars are green, and all others (F stars, cooler horizontal-branch stars) are red. Note that the three samples do comprise different regions of color space, suggesting that purely photometric separation criteria are possible, but that the overlap between the regions is quite significant. The sequence of theoretical horizontal-branch models discussed in § 7 is plotted as the thick curved line. The five black circles on the thick line denote (from the top down and to the left) stars with absolute magnitudes $g = 0.6, 0.55, 0.6, 0.7$, and 0.8 .

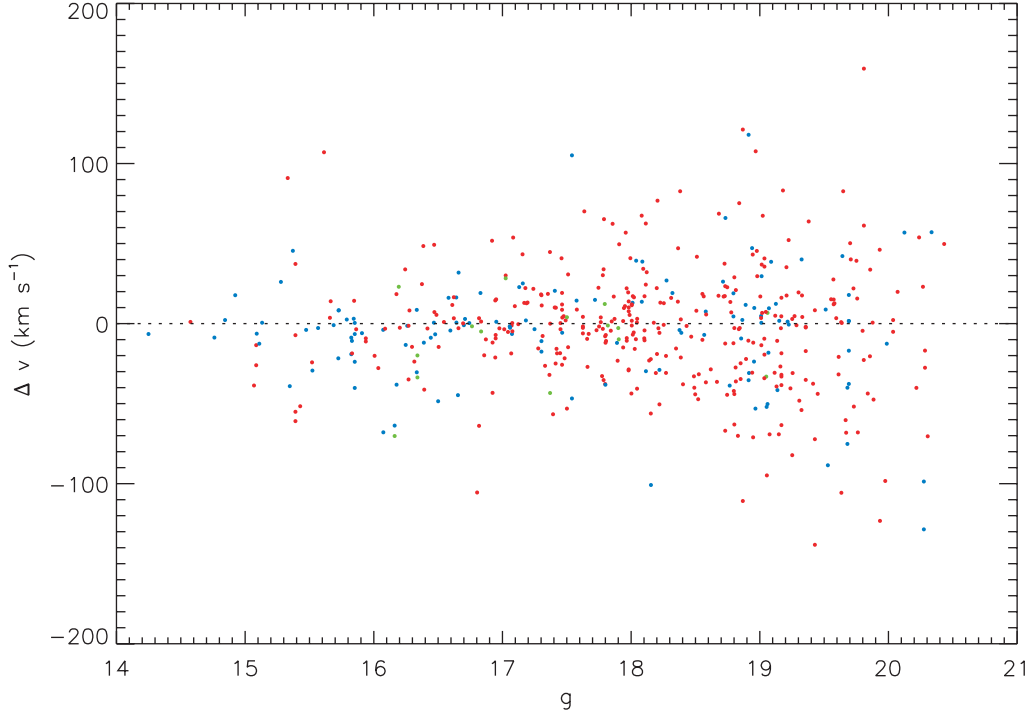


FIG. 9.—Discrepancies between the radial velocity determinations Δv_r from duplicate observations of the same stars vs. g magnitude. The velocity error increases for faint stars, as expected. Stars are colored blue if both observations indicate a BHB star (using the combination cut for $g < 18$ and the stringent color cut for $g > 18$), red if both indicate a non-BHB star, and green if the two observations are in conflict. The reason there are some conflicting classifications for $g > 18$ is because the two spectroscopic observations sometimes actually reference different photometric observations when available.

BHB or BS star. This comparison implies that the errors have been underestimated and this is currently under investigation. The rms of Δv_r in Figure 9 is 36.5 km s^{-1} . Clearly the errors in radial velocity measurements are not Gaussian, but a meaningful approximate result may still be obtained if they are assumed to be so. Since the distribution of Δv_r is based on the errors of two measurements, the error of one measurement is approximately $\Delta v_r \approx 36.5/\sqrt{2} \approx 26 \text{ km s}^{-1}$.

7. THE ABSOLUTE MAGNITUDE OF BHB STARS

In order to refine our photometric distance estimates, we have computed theoretical colors and bolometric corrections for BHBs. We integrate the latest Kurucz model atmospheres⁶ against the SDSS filter response functions at a standard air mass of 1.2 atm, in the manner described by Lenz et al. (1998). Unfortunately, the latter authors report only colors, so it was necessary to repeat their calculations in order to obtain the bolometric corrections. Apart from wavelength, the Kurucz spectra are functions of three parameters: effective temperature T_{eff} , surface gravity $g = GM/r^2$, and metallicity relative to solar $[M/H]$.

To derive absolute magnitudes and bolometric corrections, it is necessary to assume a relationship between the luminosity L and T_{eff} . The models of Dorman, Rood, & O’Connell (1993) for the theoretical zero-age horizontal branch (ZAHB) at $[M/H] \leq -1.5$ can be summarized roughly by

$$\log (L/L_{\odot}) \approx 1.58 - 0.73 \log (T_{\text{eff}}/10^4 \text{ K}), \quad (2)$$

over the range $8000 \text{ K} \leq T_{\text{eff}} \leq 12000 \text{ K}$. From a detailed study of the horizontal branch of M5, however, Baev, Markov, & Spassova (2001) find that luminosity varies more weakly with T_{eff} ; in fact their results appear to be consistent with constant luminosity and mass,

$$M \approx 0.6 M_{\odot}, \quad \log (L/L_{\odot}) \approx 1.65, \quad (3)$$

with a scatter of no more than $\pm 0.05 M_{\odot}$ and $\pm 0.05 \text{ dex}$, respectively, over the same temperature range. We adopt

the mean values in equation (3), so that $\log g \approx 3.52 + 4 \log (T_{\text{eff}}/10^4 \text{ K})$.

To give an idea of the theoretical uncertainties, we note that if in fact the relation (eq. [2]) holds for our HB stars, then by adopting equation (3) we have overestimated their distance moduli by an average of 0.18 mag over the indicated range of T_{eff} , and by neglecting the variation of L with T_{eff} , we have increased the scatter in distance modulus by $\approx 0.09 \text{ mag}$, which should be taken in quadrature with the photometric measurement error.

The results of this exercise are shown in Table 2. Evidently, for the colors of interest to us, $T_{\text{eff}} \in (8000, 12000) \text{ K}$, and the influence of metallicity is slight if $[M/H] \leq -1$.

The sequence of theoretical horizontal-branch stars, parametrized by temperature, is projected onto the $(u-g, g-r)$ -plane in Figure 8. The five black circles on the thick line denote, starting at the top and progressing down and to the left, stars with absolute magnitudes $g = (0.6, 0.55, 0.6, 0.7, 0.8)$. For every observed BHB star in our sample (colored blue in the figure) we define the most probable absolute magnitude associated with its $(u-g, g-r)$ colors by simply finding the absolute magnitude of the point on the theoretical track that is closest to the observed star in this color-color space.

The stringent color cut (piano shape in Fig. 8; see § 5) was defined before the theoretical track was calculated, so the fact that the theoretical track satisfies the stringent color cut is a meaningful consistency check.

As a further consistency check, we have isolated several Galactic globular clusters observed by the SDSS photometric survey to date and plotted their color-magnitude diagrams (CMDs). Pal 3, NGC 5904, and NGC 6205 do not show a discernible horizontal branch, so they are not considered here. The g versus $g-r$ CMDs of Pal 5 (Yanny et al. 2000; Ivezić et al. 2000) and NGC 2419 are presented in Figure 10, in which the distance modulus, derived from cluster distances of $d = 84.2$ and 23.2 kpc for NGC 2419 and Pal 5, respectively (Harris 1996), has been subtracted from the dereddened apparent magnitude g . Stars within $8'$ of the center of NGC 2419 and within $14'$ of the center of Pal 5 were selected. The SDSS automated photometry avoids analyzing very crowded fields, so the stars presented here, though within the stated radii, tend

TABLE 2
PREDICTED ABSOLUTE MAGNITUDES AND COLORS FOR BLUE HORIZONTAL-BRANCH STARS
IN THE SDSS SYSTEM

T_{eff}	$\log g$	g (10 pc)	$u-g$	$g-r$	$g-i$
7000.....	2.900	0.7115 0.6862	1.0335 1.0836	0.0945 0.0999	0.0736 0.0724
8000.....	3.132	0.5712 0.5494	1.1792 1.1944	-0.1313 -0.1291	-0.2700 -0.2724
9000.....	3.336	0.6311 0.6121	1.0695 1.0732	-0.2300 -0.2317	-0.4301 -0.4351
10000.....	3.520	0.8000 0.7753	0.8911 0.8853	-0.2742 -0.2780	-0.5023 -0.5093
11000.....	3.685	0.9954 0.9672	0.7381 0.7239	-0.2999 -0.3034	-0.5449 -0.5512
12000.....	3.836	1.1884 1.1582	0.6139 0.5950	-0.3203 -0.3232	-0.5785 -0.5836
13000.....	3.975	1.3735 1.3425	0.5103 0.4881	-0.3382 -0.3404	-0.6075 -0.6115

NOTES.—Assuming eq. (3) and $[M/H] = -2.0$ (first line at each T_{eff}) and $[M/H] = -1.0$ (second line). In the second column g is gravity; in all other instances it is the magnitude in the g band.

⁶ See <http://www.kurucz.harvard.edu>.

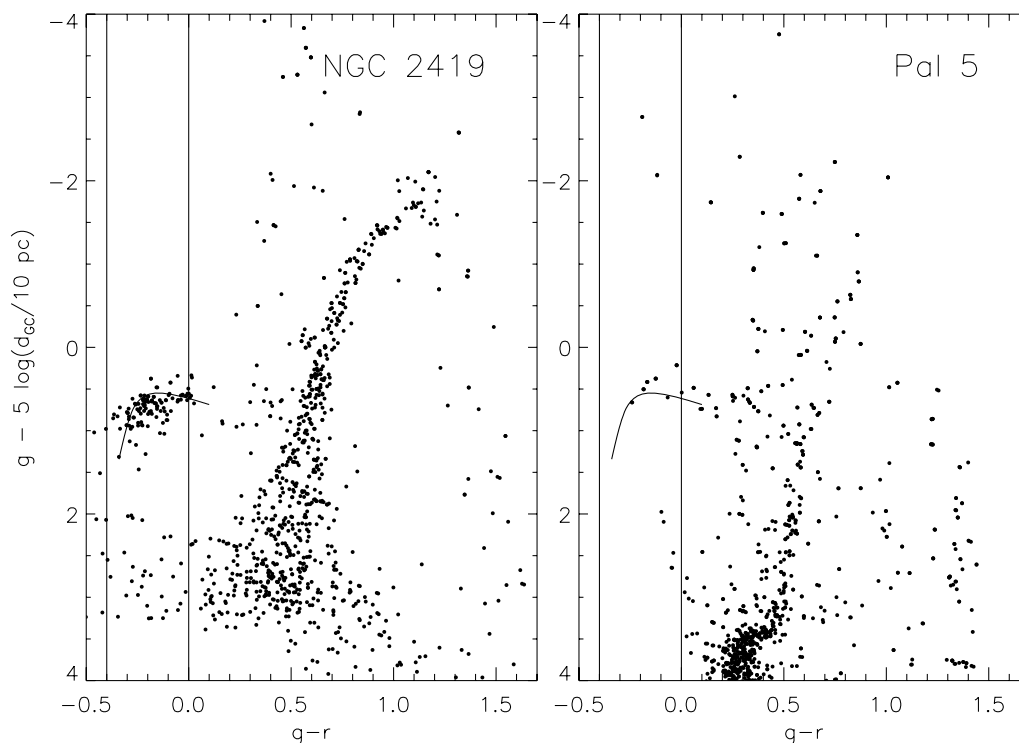


FIG. 10.—Color-magnitude diagrams for the Galactic globular clusters NGC 2419 and Pal 5. The distance modulus has been subtracted from the dereddened g magnitudes to arrive at directly observed absolute magnitudes. Lines at $g-r = (-0.4, 0.0)$ denote the color cut. The theoretical horizontal-branch sequence is overplotted.

to lie in the outskirts of the clusters. Vertical lines at $g-r = (-0.4, 0.0)$ indicate our color cut. The theoretical horizontal-branch sequence is also plotted in both panels. The horizontal-branch stars of NGC 2419 appear to be systematically fainter than the theoretical prediction, while those of Pal 5 seem to be systematically brighter; however, these systematic differences could easily be due to inaccurate distances d . By selecting from these two globular clusters the stars passing the color cut ($0.8 < u-g < 1.35$, $-0.4 < g-r < 0.0$) and lying in the region of the CMD for the horizontal branch [$0.0 < g - 5 \log(d/10 \text{ pc}) < 1.5$], we compare the directly observed absolute magnitude $g - 5 \log(d/10 \text{ pc})$ to the indirectly obtained theoretical absolute magnitude based on the $(u-g, g-r)$ colors. For NGC 2419, the rms of the differences of the two among the 94 stars is 0.134 mag, and the root sum square (rss) is 0.167 mag.⁷ For Pal 5, the rms is 0.126 mag and the rss is 0.202 mag. The difference between the rms and rss is due to the nonzero mean, or systematic error as discussed above. Therefore, the magnitude error of a star, with absolute magnitude determined by comparison with the theoretical horizontal-branch sequence described above, is on the order of 0.2 mag. The error may be as small as ~ 0.13 mag if the only cause of the systematic difference between directly observed absolute magnitudes and our indirectly obtained absolute magnitudes is incorrect distances for Pal 5 and NGC 2419.

8. SANITY CHECKS

As Figure 8 shows, BHB stars determined by the combination cut are in general redder in $u-g$ and bluer in $g-r$ than

other objects such as BS stars. This result is consistent with the work of Yanny et al. (2000), so it is reassuring. In this section we present several more sanity checks that verify that our sample of BHB stars is probably accurate.

8.1. Metallicity from the Ca II K Line

BHB stars are halo stars, and as such they should have lower metallicity than the disk star contaminants. The most promising spectral feature to use for a metallicity determination is the Ca II K line at 3933.7 Å (the H line at 3968.5 Å is

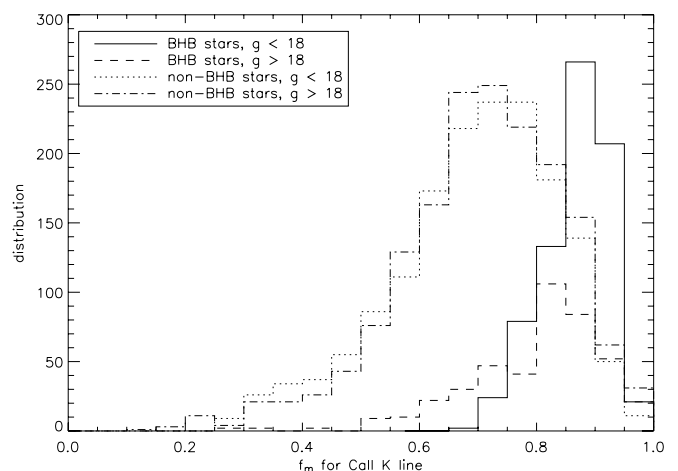


FIG. 11.—Distribution of the f_m parameter for the Ca II K line for BHB stars and non-BHB stars. Although BHB stars clearly have larger values of f_m and thus lower metallicity implying that they are halo objects, they are not so clearly separated from the non-BHB stars. This is probably because SDSS spectroscopy does not have a high enough resolution and S/N to probe the Ca II K line as accurately as it can the Balmer H γ and H δ lines.

⁷ That is, $\text{rms} = [N^{-1} \sum (\Delta g_i - \langle \Delta g \rangle)^2]^{1/2}$, $\langle \Delta g \rangle = (\sum \Delta g_i)/N$, $\text{rss} = (N^{-1} \sum \Delta g_i^2)^{1/2}$.

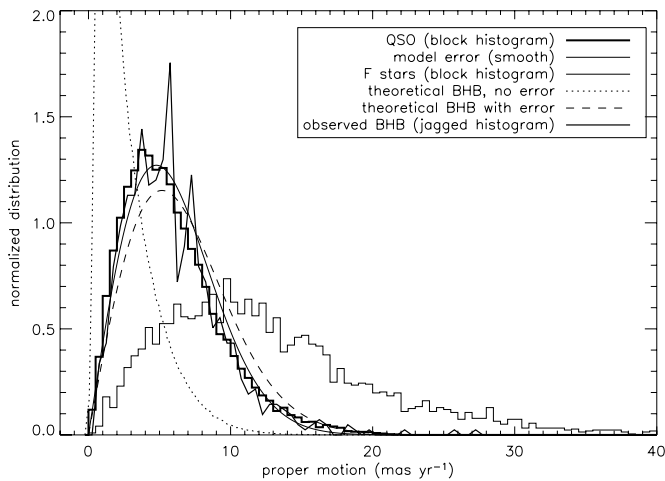


FIG. 12.—Distributions of measured proper motion of SDSS objects, with integrals normalized to unity, of SDSS objects compared to USNO catalogs. The QSO histogram reflects measurement error. The smooth thin curve is the expected analytic form from eq. (4) of the QSO distribution with variance $(4.77 \text{ mas yr}^{-1})^2$. Our sample of 1170 BHB stars is plotted as jagged (not boxy) for clarity. The dotted line is the expected distribution of true proper motions for the BHB sample. The dashed curve is the expected *measured* distribution of BHBs given the theory of measurement errors described in the text. The close match between the QSOs and BHB stars qualitatively indicates that contamination from foreground objects is low.

not used because it is too close to He). Unfortunately, it is impractical to use the Ca II K line as a *reliable* indicator of metallicity in individual SDSS spectra because much higher spectral resolution would be necessary. However, the following exercise is executed anyway as a sanity check. By employing a continuum-subtraction algorithm very similar to that described in § 4.1 for the $\text{H}\gamma$ and $\text{H}\delta$ Balmer lines, we find the value of f_m for the Ca II K line; smaller values indicate larger metallicity. Figure 11 presents the distributions of this parameter for our sample of BHB stars and non-BHB stars passing the color cut. The figure shows different distributions for bright ($g < 18$) and faint ($g > 18$) stars because of the difference in S/N. Reassuringly, our BHB stars tend to have lower metallicities.

8.2. Proper Motion

The proper motions of objects in SDSS are found automatically by matching the stellar positions to those in the astrometric catalog USNO-A2.0 (Monet et al. 1998) derived from the digitized Palomar Observatory Sky Survey (POSS) plates, for objects bright enough to have a POSS counterpart. The normalized distribution of the proper motion of spectroscopically confirmed quasi-stellar objects (QSOs) is shown in Figure 12 as a thick line. These alleged proper motions of QSOs are obviously due to measurement errors, both from the POSS and SDSS (primarily from the former). If both

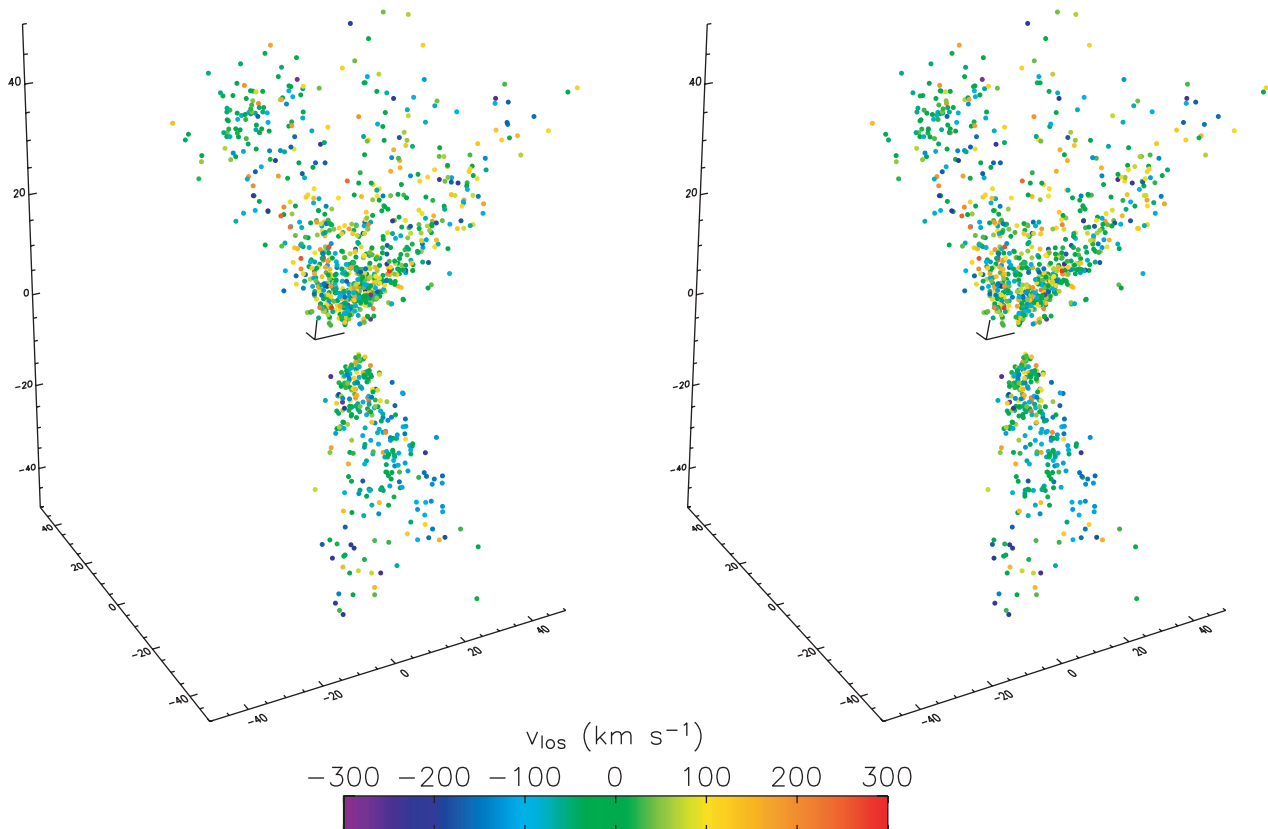


FIG. 13.—Two three-dimensional projections of BHB stars discovered by the SDSS spectroscopic survey, comprising a stereograph that can be viewed in three dimensions by focusing the eyes on a point midway to the paper or with a stereoscope. Each star is colored according to its line-of-sight radial velocity with the solar velocity subtracted out. One can search for substructure in the halo by looking for streamers in this figure. Although substructure is not the emphasis for this work, we note the lump in the upper left, which is the Sagittarius dwarf tidal stream. The bracket in the middle of the figure represents a coordinate system centered on the Galactic center with the longest line segment pointing toward and terminating at the location of the Sun at 8 kpc. Galactic north is up. Only stars within a cube of half-length 50 kpc are drawn. The axes are labeled in kiloparsecs.

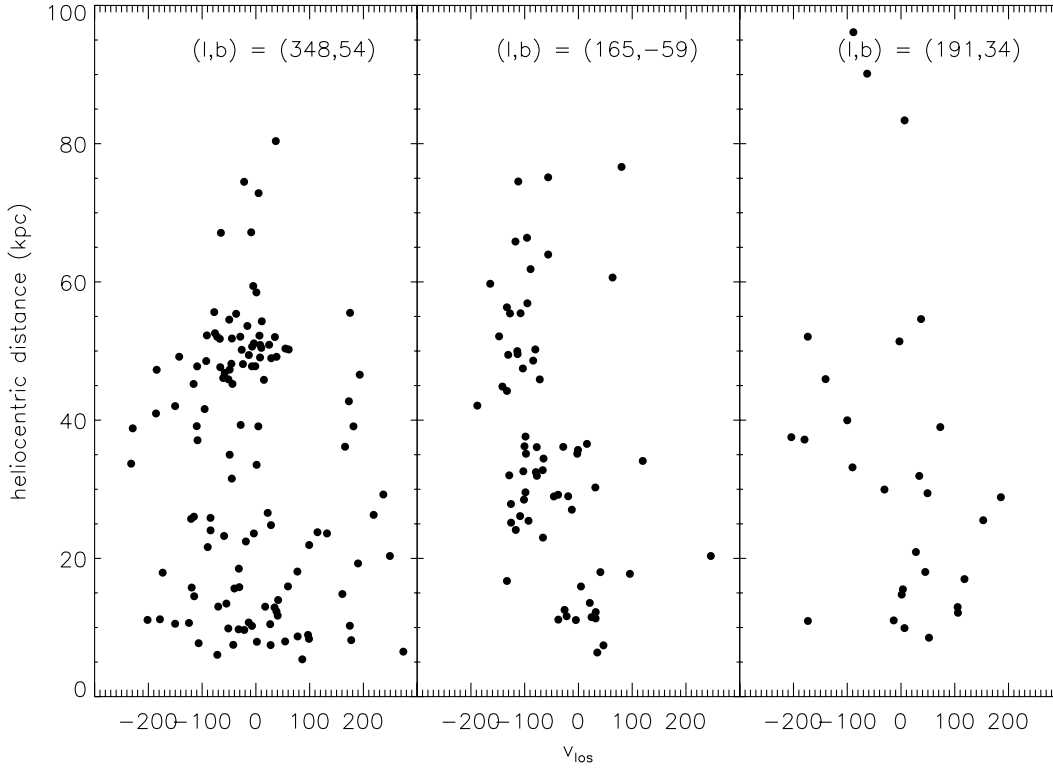


FIG. 14.—Phase space plots for three subsamples of the BHB sample extracted from the Sagittarius stream. The three regions of extraction are given by the intersection of the BHB sample with the 10° wide strip following the great circle described in § 8.3. The left plot, from the north Galactic cap, clearly shows a clump in phase space at ~ 50 kpc, which represents the Sagittarius stream. The middle plot, from the south, can also be seen to show similar structure. The right plot is from the north but the number of stars is too small to draw any conclusions about the detection of the Sagittarius stream in this region of space.

measurements follow bivariate Gaussian errors with radially symmetric variances σ_1^2 and σ_2^2 , then the distribution of the separation of the measurements (i.e., proper motion) also follows a bivariate Gaussian with variance $\sigma^2 = \sigma_1^2 + \sigma_2^2$. Thus, the probability density distribution of observing a star with true proper motion μ_0 at an observed proper motion μ is

$$\begin{aligned} \phi_{\mu_0}(\mu) &= \frac{1}{2\pi\sigma^2} \int_0^{2\pi} \exp\left(-\frac{\mu^2 + \mu_0^2 - 2\mu\mu_0 \cos \theta}{2\sigma^2}\right) \mu d\theta \\ &= \frac{\mu}{\sigma^2} \exp\left(-\frac{\mu^2 + \mu_0^2}{2\sigma^2}\right) I_0\left(\frac{\mu\mu_0}{\sigma^2}\right), \end{aligned} \quad (4)$$

where $I_0(x)$ is the modified Bessel function of the first kind. Since $\mu_0 \rightarrow 0$ for the QSO distribution, the second moment of the distribution of μ should equal $2\sigma^2$ for Gaussian statistics. This determination yields $\sigma_{\text{QSO}} = 4.77 \text{ mas yr}^{-1}$, and the resulting theoretical error distribution function from equation (4) is shown in Figure 12 as a thin line.

We have estimated the statistical intrinsic proper motions of our sample using the derived photometric distances. The transverse velocity of each star was drawn 1000 times at random from an isotropic velocity distribution with dispersion 100 km s^{-1} in one dimension and corrected for an assumed solar velocity $\mathbf{v}_\odot = (10, 225, 7) \text{ km s}^{-1}$ (Dehnen & Binney 1998). These choices were based on the kinematic results presented in Paper II. The distribution of intrinsic proper motions so derived, $N(\mu_0)$, is shown in Figure 12 as the dotted line. The theoretical proper motion distribution

for BHB stars with measurement errors should follow the form

$$\phi_{\text{BHB}}(\mu) \propto \int_0^\infty N(\mu_0) \phi_{\mu_0}(\mu) d\mu_0 \quad (5)$$

and is drawn in Figure 12 as the dashed line. The distribution of *measured* proper motions of our BHB sample is also shown. This distribution is clearly not very much broader than that of the QSOs; the second moment yields $\sigma_{\text{BHB}} = 4.84 \text{ mas yr}^{-1}$, which is actually too small to account for the combination of measurement error ($\sigma_{\text{QSO}} = 4.77 \text{ mas yr}^{-1}$) and intrinsic proper motion ($\sigma_{\text{BHB int}} = 2.32 \text{ mas yr}^{-1}$)! In contrast, the proper motion distribution of a sample of faint (here $r > 16.7$) F stars from SDSS is also shown, with a much broader distribution. This finding demonstrates that contamination in the BHB sample from F stars must be very small. We estimate that the F star contamination is less than 5% among the 837 stars in our sample that were matched to USNO-A. Without a better understanding of systematic errors, we cannot claim to have detected proper motion of the BHB sample. However, the USNO-B catalog, which has appreciably better data quality than USNO-A, will soon be provided as the first epoch for proper motions, so we defer further analysis to later work.

8.3. A Map of the Galactic Halo and the Sagittarius Dwarf Tidal Stream

Figure 13 shows two views of a three-dimensional representation of the locations of the BHB stars. Each star is

TABLE 3
LIST OF 1170 BHB STARS SELECTED FROM SDSS

ASTROMETRY				UNCORRECTED MAGNITUDES					EXTINCTION-CORRECTED MAGNITUDES				
R.A.	Decl.	ℓ	b	u	g	r	i	z	u	g	r	i	z
145.82320	−1.17255	237.13901	36.66249	17.89	16.68	16.85	16.95	17.04	17.65	16.50	16.73	16.86	16.97
160.36295	−1.05517	249.66811	47.91172	18.08	16.83	16.91	16.94	17.06	17.80	16.62	16.76	16.83	16.98
161.66508	0.06255	249.84621	49.62371	18.55	17.20	17.36	17.47	17.50	18.34	17.05	17.25	17.39	17.44
161.08659	1.00213	248.17850	49.86035	18.64	17.37	17.40	17.51	17.55	18.41	17.20	17.28	17.42	17.48
161.20377	0.68167	248.66331	49.72445	17.88	16.60	16.72	16.81	16.89	17.65	16.43	16.60	16.72	16.82

REDSHIFT	v_{los}	D (kpc)	$D_{0.2}$ METHOD PARAMETERS					SCALE WIDTH-SHAPE PARAMETERS			
			$D_{0.2,\text{H}\gamma}$	$f_{m,\text{H}\gamma}$	$D_{0.2,\text{H}\delta}$	$f_{m,\text{H}\delta}$	$f_{m,\text{Ca II}}$	$b_{\text{H}\gamma}$	$c_{\text{H}\gamma}$	$b_{\text{H}\delta}$	$c_{\text{H}\delta}$
0.0005883	24.71	15.34	27.3646	0.3316	25.6610	0.2890	0.9099	11.5214	1.1931	11.2208	1.1947
0.0005751	33.98	16.36	25.9615	0.3286	28.0140	0.2953	0.8329	11.0010	1.1813	11.9872	1.0941
0.0005553	32.86	19.98	24.1510	0.3700	27.3331	0.3313	0.8483	10.4411	1.0110	10.8343	0.9828
0.0008044	109.62	21.27	23.5976	0.3580	27.3562	0.3028	0.8724	9.3291	1.0594	11.6956	0.9662
0.0006674	67.72	14.98	26.9836	0.3368	26.8800	0.3101	0.7589	10.5769	1.0842	11.7013	1.0022

NOTES.—The first four columns contain the astrometry (R.A., decl., ℓ , b) for each object. The magnitudes (u , g , r , i , z) are in the next 10 columns: uncorrected and corrected for extinction. The heliocentric redshift is listed next. The next column is v_{los} , the galactocentric velocity in kilometers per second, assuming $\mathbf{v}_{\odot} = (10, 225, 7) \text{ km s}^{-1}$. The next column is the distance in kiloparsecs as determined by the method described in § 7. The last nine columns are the line width parameters from the Balmer and Ca II lines. Table 3 is presented in its entirety in the electronic edition of the *Astronomical Journal*. A portion is shown here for guidance regarding its form and content.

colored according to its line-of-sight radial velocity with the solar velocity of $(10, 225, 7) \text{ km s}^{-1}$ (Dehnen & Binney 1998) added. These two views compose a stereograph, which can be viewed by focusing the eyes on a point midway to the paper. The three-dimensional positions of the stars are derived from their angular positions and photometric distances (§ 7), assuming $R_0 = 8 \text{ kpc}$.

One could search for substructure in the Galactic halo by a careful examination of Figure 13, and indeed a clump appears in the top left part of the plot [at $(l, b) \sim (350, 50)$]. This clump belongs to the leading arm of the Sagittarius dwarf tidal stream (Ivezić et al. 2000; Yanny et al. 2000; Ibata et al. 2001a, 2001b). It is interesting to investigate this structure in velocity phase space, as shown in Figure 14. The Sagittarius stream approximately follows the great circle on the celestial sphere with pole $(\alpha, \delta) = (308, 58)$ or $(l, b) = (94, 11)$, as determined from the distribution of SDSS candidate RR Lyrae stars. Practically the same position is implied by the distribution of 2MASS M giants (Majewski et al. 2003). This great circle intersects the footprint of the SDSS in three places. These three intersections with BHB stars (two in the north and one in the south, with a strip width of 10°) are represented in the three panels in Figure 14. One can see a clump in the phase space of the northern subsample representing the Sagittarius stream (*left plot*); indeed it is the same clump in the top left of Figure 13. The coherent structure in the middle panel (at $D \sim 30 \text{ kpc}$) is also associated with the Sgr dwarf tidal stream (trailing arm). This is the same clump that was discovered by Yanny et al. (2000) using A-colored stars, and is also detected in the velocity-distance distribution of SDSS candidate RR Lyrae stars (Ivezić et al. 2003). The fact that we see such structure in the BHB sample strongly indicates that our BHB absolute magnitudes and selection criteria are reliable.

9. SUMMARY

Using broadband colors and spectroscopic surface-gravity indicators, we have selected 1170 blue horizontal-branch stars

from the SDSS. For the 733 bright stars ($g < 18$) the contamination is probably $\lesssim 10\%$, and for the 437 faint BHB stars ($g > 18$) the contamination is probably $\sim 25\%$. The absolute magnitude of BHB stars was determined from globular cluster color-magnitude diagrams, and an absolute-magnitude-color relation established. This was used to estimate photometric distances, with errors $\approx 0.2 \text{ mag}$. The stars also have measured radial velocities with errors $\approx 26 \text{ km s}^{-1}$. Proper motions determined by matching against the digitally scanned Palomar Sky Survey (USNO-A; Monet et al. 1998) also indicate that contamination from the disk is small. We emphasize, however, that no kinematic information was used to select the sample. The data can be downloaded as Table 3 in the electronic version of this paper.

We thank A. Gould, B. Paczyński, R. Lupton, and J. Hennawi for helpful discussions and M. Strauss for a close reading of a draft of this paper. G. R. K. is grateful for generous research support from Princeton University and from NASA via grants NAG-6734 and NAG5-8083. Funding for the creation and distribution of the SDSS Archive has been provided by the Alfred P. Sloan Foundation, the Participating Institutions, the National Aeronautics and Space Administration, the National Science Foundation, the US Department of Energy, the Japanese Monbukagakusho, and the Max Planck Society. The SDSS Web site is <http://www.sdss.org>. The SDSS is managed by the Astrophysical Research Consortium (ARC) for the Participating Institutions. The Participating Institutions are the University of Chicago, Fermilab, the Institute for Advanced Study, the Japan Participation Group, The Johns Hopkins University, Los Alamos National Laboratory, the Max Planck Institute for Astronomy, the Max Planck Institute for Astrophysics, New Mexico State University, the University of Pittsburgh, Princeton University, the US Naval Observatory, and the University of Washington.

APPENDIX

REMARK ON CONTAMINATION AND INCOMPLETENESS

There is no independently confirmed subsample of BHB stars, but we can estimate the accuracy of our spectroscopic selection methods by intercomparing their results.

After applying our color cut, we are left with $N + C = 2338$ candidates bright enough to be subjected to our spectroscopic selection criteria. Of these, N are true BHB stars, and the other C are potential contaminants. Let $\eta_i \leq 1$ be the probability that method i fails to identify a true BHB as such and κ'_i be the probability that it mistakenly accepts an individual member of the non-BHB group. Then the expected number of stars accepted by method i is

$$N_i = (1 - \eta_i)N + \kappa'_i C. \quad (\text{A1})$$

Similarly, the number of stars selected jointly by methods i and j , or by i, j , and k , is

$$\begin{aligned} N_{i \cap j} &= (1 - \eta_i)(1 - \eta_j)N + \kappa'_i \kappa'_j C, \\ N_{i \cap j \cap k} &= (1 - \eta_i)(1 - \eta_j)(1 - \eta_k)N + \kappa'_i \kappa'_j \kappa'_k C, \end{aligned}$$

respectively, assuming that these methods are truly independent. (See Table 4 for a list of the numbers of stars that are selected jointly.) It is convenient to define $\kappa_i \equiv \kappa'_i C / N_i$ so that the number of contaminants among the N_i stars accepted by method i is $\kappa_i N_i$. Then

$$N_i = \frac{(1 - \eta_i)}{(1 - \kappa_i)} N, \quad (\text{A2})$$

$$N_{i \cap j} = \left[\frac{(1 - \kappa_i)(1 - \kappa_j)}{N} + \frac{\kappa_i \kappa_j}{C} \right] N_i N_j, \quad (\text{A3})$$

$$N_{i \cap j \cap k} = \left[\frac{(1 - \kappa_i)(1 - \kappa_j)(1 - \kappa_k)}{N^2} + \frac{\kappa_i \kappa_j \kappa_k}{C^2} \right] N_i N_j N_k. \quad (\text{A4})$$

As described in § 4, we have four methods. Therefore, we have six double intersections (eq. [A3]) and four triple intersections (eq. [A4]) with which to solve for the six unknown parameters ($\kappa_1, \dots, \kappa_4, N, C$) that they contain. So the problem is overdetermined, allowing us perhaps to test the assumption of independence. Perfect consistency is not to be expected since even for fixed values of the above parameters, the numbers $\{N_i, N_{i \cap j}, N_{i \cap j \cap k}\}$ are subject to statistical fluctuations.

TABLE 4
NUMBERS OF STARS JOINTLY SELECTED

$D_{0.2}(\text{H}\gamma)$	$D_{0.2}(\text{H}\delta)$	SW-S (H γ)	SW-S (H δ)	$N_i, N_{i \cap j}, \dots$
0	0	0	0	2338
0	0	0	1	741
0	0	1	0	746
0	0	1	1	683
0	1	0	0	779
0	1	0	1	661
0	1	1	0	658
0	1	1	1	620
1	0	0	0	777
1	0	0	1	670
1	0	1	0	692
1	0	1	1	642
1	1	0	0	673
1	1	0	1	620
1	1	1	0	630
1	1	1	1	595

NOTES.—The first four columns are binary bits indicating which selection methods were applied. The first row gives the total number of candidate stars ($g < 18$); the last row gives the number selected by all four methods.

TABLE 5
ACCURACY OF FOUR SPECTROSCOPIC SELECTION METHODS

METHOD i (1)	Est. of κ_i (2)	Est. of κ_i (3)	Est. of κ_i (4)	$\langle \kappa_i \rangle$ (5)	$\langle \eta_i \rangle$ (6)
$D_{0.2}(\text{H}\gamma)$	0.0706	0.0640	0.0486	0.0611	0.0552
$D_{0.2}(\text{H}\delta)$	0.0995	0.0789	0.0977	0.0920	0.0840
SW-S($\text{H}\gamma$)	0.0283	0.0131	0.0312	0.0242	0.0573
SW-S($\text{H}\delta$)	0.0173	0.0381	0.0360	0.0305	0.0696

NOTES.—Estimates in cols. (2)–(4) are based on the three triples involving i drawn from methods 1, 2, 3, and 4 (eq. [A5]), col. (5) is their average, and col. (6) is computed from col. (5) and eq. (A2).

If the contamination fractions κ_i are reasonably small—it is sufficient that $\kappa/(1 - \kappa) \ll (C/N)^{1/2}$ —then the terms involving C in equations (A3)–(A4) are unimportant, so that

$$1 - \kappa_i \approx \frac{N_{i \cap j} N_{i \cap k}}{N_{i \cap j \cap k} N_i}. \quad (\text{A5})$$

This approach yields the results shown in Table 5, and also an estimate for the true number of BHBs tested (i.e., not including those too faint for spectroscopic selection): $N \approx 772$. Note that there are three possible choices of (j, k) with which to estimate κ_i from equation (A5), all of which are shown in the table to give an idea of their consistency. It can be seen that the contamination and incompleteness fractions for each are indeed small, $<10\%$, if these methods are indeed independent as we have assumed. In support of the latter, the differences among the estimates in columns (2)–(4) are about ± 0.01 as would be expected by chance since, for example, binomial statistics predict that the number of false negatives for method i should fluctuate by $\pm [\eta_i(1 - \eta_i)N]^{1/2}$, or about seven out of 772 if $\eta_i = 0.07$.

REFERENCES

- Abazajian, K., et al. 2003, *AJ*, 126, 2081
 Arnold, R., & Gilmore, G. 1992, *MNRAS*, 257, 225
 Baev, P. V., Markov, H., & Spassova, N. 2001, *MNRAS*, 328, 944
 Clewley, L., Warren, S. J., Hewett, P. C., Norris, J. E., Peterson, R. C., & Evans, N. W. 2002, *MNRAS*, 337, 87
 Dehnen, W., & Binney, J. J. 1998, *MNRAS*, 298, 387
 Dorman, B., Rood, R. T., & O'Connell, R. W. 1993, *ApJ*, 419, 596
 Eisenstein, D. J., et al. 2001, *AJ*, 122, 2267
 Flynn, C., Sommer-Larsen, J., & Christensen, P. R. 1994, *MNRAS*, 267, 77
 Fukugita, M., Ichikawa, T., Gunn, J. E., Doi, M., Shimasaku, K., & Schneider, D. P. 1996, *AJ*, 111, 1748
 Gunn, J. E., Carr, M., Rockosi, C., & Sekiguchi, M., et al. 1998, *AJ*, 116, 3040
 Harris, W. E. 1996, *AJ*, 112, 1487
 Hogg, D. W., Finkbeiner, D. P., Schlegel, D. J., & Gunn, J. E. 2001, *AJ*, 122, 2129
 Ibata, R., Irwin, M., Lewis, G. F., & Stolte, A. 2001a, *ApJ*, 547, L133
 Ibata, R., Lewis, G. F., Irwin, M., Totten, E., & Quinn, T. 2001b, *ApJ*, 551, 294
 Ivezić, Ž., et al. 2000, *AJ*, 120, 963
 ———. 2003, *ASP Conf. Ser.*, *Milky Way Surveys, the Structure and Evolution of Our Galaxy*, ed. D. Clemens & T. Brainerd (San Francisco: ASP), in press
 Kinman, T. D., Suntzeff, N. B., & Kraft, R. P. 1994, *AJ*, 108, 1722
 Layden, A. C., Hanson, R. B., Hawley, S. L., Klemola, A. R., & Hanley, C. J. 1996, *AJ*, 112, 2110
 Lenz, D. D., Newberg, J., Rosner, R., Richards, G. T., & Stoughton, C. 1998, *ApJS*, 119, 121
 Lupton, R. H., Gunn, J. E., Ivezić, Z., Knapp, G. R., Kent, S., & Yasuda, N. 2001, in *ASP Conf. Ser.* 238, *Astronomical Data Analysis Software and Systems X*, ed. F. R. Harden, Jr., F. A. Primini, & H. E. Payne (San Francisco: ASP), 269
 Majewski, S., Skrutskie, M. F., Weinberg, M. D., & Ostheimer, J. C. 2003, *ApJ*, 599, 1082
 Monet, D. B. A., et al. 1998, *USNO-A2.0 Catalog* (Washington: US Naval Observatory)
 Pier, J. R. 1983, *ApJS*, 53, 791
 ———. 1984, *ApJ*, 281, 260
 Pier, J. R., Munn, J. A., Hindsley, R. B., Hennessy, G. S., Kent, S. M., Lupton, R. H., & Ivezić, Ž. 2003, *AJ*, 125, 1559
 Preston, G. W., & Sneden, C. 2000, *AJ*, 120, 1014
 Prugniel, P., & Soubiran, C. 2001, *A&A*, 369, 1048
 Richards, G. T., et al. 2002, *AJ*, 123, 2945
 Schlegel, D. J., Finkbeiner, D. P., & Davis, M. 1998, *ApJ*, 500, 525
 Sérsic, J. L. 1968, *Atlas de galaxies australes* (Cordoba, Argentina: Obs. Astron.)
 Sirko, E., et al. 2004, *AJ*, 127, 914 (Paper II)
 Smith, J. A., et al. 2002, *AJ*, 123, 2121
 Sommer-Larsen, J., Beers, T. C., Flynn, C., Wilhelm, R., & Christensen, P. R. 1997, *ApJ*, 481, 775
 Sommer-Larsen, J., & Christensen, P. R. 1986, *MNRAS*, 219, 537
 Sommer-Larsen, J., Christensen, P. R., & Carter, D. 1989, *MNRAS*, 238, 225
 Stoughton, C., et al. 2002, *AJ*, 123, 485
 Strauss, M. A., et al. 2002, *AJ*, 124, 1810
 Wilhelm, R., Beers, T. C., & Gray, R. O. 1999, *AJ*, 117, 2308
 Yanny, B., et al. 2000, *ApJ*, 540, 825
 York, D. G., et al. 2000, *AJ*, 120, 1579